Photonic spin-orbit coupling induced by deep-subwavelength structured light

Xin Zhang,[1,2] Guohua Liu,[1,2] Yanwen Hu,[1,2,3,*] Haolin Lin,[1,2] Zepei Zeng,[1,2] Xiliang Zhang,[1,2] Zhen Li,[1,2,3] Zhenqiang Chen,[1,2,3] and Shenhe Fu[1,2,3,†]

[1]*Department of Optoelectronic Engineering, Jinan University, Guangzhou 510632, China*
[2]*Guangdong Provincial Key Laboratory of Optical Fiber Sensing and Communications, Guangzhou 510632, China*
[3]*Guangdong Provincial Engineering Research Center of Crystal and Laser Technology, Guangzhou 510632, China*

(Received 18 May 2023; accepted 1 February 2024; published 20 February 2024)

We demonstrate both theoretically and experimentally beam-dependent photonic spin-orbit coupling in a two-wave mixing process described by an equivalent of the Pauli equation in quantum mechanics. The considered structured light in the system is comprising a superposition of two orthogonal spin-orbit-coupled states defined as spin-up and -down equivalents. The spin-orbit coupling is manifested by prominent pseudospin precession as well as spin-transport-induced orbital angular momentum generation in a photonic crystal film of wavelength thickness. The coupling effect is significantly enhanced by using a deep-subwavelength carrier envelope, different from previous studies which depend on materials. The beam-dependent coupling effect can find intriguing applications; for instance, it is used in precisely measuring variation of light with spatial resolution up to 15 nm.

DOI: 10.1103/PhysRevA.109.023522

I. INTRODUCTION

Spin-orbit coupling (SOC), which refers to interaction of a quantum particle's spin with its momentum, is a fundamentally important concept. It has been extensively investigated in condensed matter physics [1,2], atomic and molecular physics [3,4], and contributes to exciting phenomena such as the spin Hall effect [5] and topological insulators [6,7]. Analogous photonic SOC is also demonstrated in a variety of settings [8]. The photonic SOC refers to an interaction between the momentum of light, which also includes spin angular momentum and orbital angular momentum (SAM and OAM). Whereas the SAM is associated with photon circular polarization [9], the OAM is relevant to a helical wavefront of light characterized by a topological number ℓ [10]. The photonic SOC is crucial for the optical Hall effects [11–14], spin-to-orbital angular momentum conversions [15,16], spin-orbit photonic devices [17–19], etc.

The SOC can be engineered in appropriately designed materials. For example, engineering a tensional strain in graphene shifts the electronic dispersions and induces a controllable vector potential for the electronic SOC [20–24]. Analogous strategy can be applied to engineer the photonic SOC, by using strained evanescently coupled waveguide arrays [25,26]. Other approaches for manipulating the photonic SOCs are demonstrated by appropriately designing microcavities [27–32], metamaterials [33–36], photonic crystals [37–39], twisted optical fibers [40,41], dual-core waveguides [42,43], etc. The resultant SOCs are material dependent, determined by geometric configurations of the materials which are often difficult to be tuned once fixed by designs. As a consequence, a tunable photonic SOC process remains elusive. Recently, several engineered photonic SOC schemes have been reported, by either embedding a strained honeycomb metasurface inside a cavity waveguide [44] or using an optical cavity filled with controllable liquid crystals [45]. However, the resultant photonic SOCs remain material dependent.

In this work, we report theoretically and experimentally a mechanism for engineering the photonic SOC. We demonstrate this by exploiting analogy between quantum description of a spin-$\frac{1}{2}$ system and a spin-orbit Hamiltonian derived for structured light in a photonic crystal. The obtained Hamiltonian is closely relevant to structured light, which means that the SOC can be engineered by controlling carrier envelope rather than the structures of materials. Strong SOC is achieved by using deep-subwavelength structured light, as manifested by clear pseudospin precessions. Although the structured light has been extensively investigated in recent years [46–51], the dependence of the photonic SOC on its spatial structure remains unnoticed.

II. THEORETICAL MODEL

We consider a two-wave mixing process involving two interacting photonic states. The SOC takes place in a crystal, represented by its principal refractive index: n_x, n_y, and n_z. With an approximation of the slowly varying envelope along optical axis z, a coupled-wave equation for the process is given by [52]

$$2i\beta_x\frac{\partial E_x}{\partial z}+\frac{n_x^2}{n_z^2}\frac{\partial^2 E_x}{\partial x^2}+\frac{\partial^2 E_x}{\partial y^2}=\gamma_y\frac{\partial^2 E_y}{\partial y\partial x}\exp\left(+i\Delta\beta z\right),$$
$$2i\beta_y\frac{\partial E_y}{\partial z}+\frac{n_y^2}{n_z^2}\frac{\partial^2 E_y}{\partial y^2}+\frac{\partial^2 E_y}{\partial x^2}=\gamma_x\frac{\partial^2 E_x}{\partial x\partial y}\exp\left(-i\Delta\beta z\right), \quad (1)$$

where $E_{x,y}$ are linearly polarized fields, and $\beta_{x,y}=k_0 n_{x,y}$ denote their propagation constants. $k_0=2\pi/\lambda$ is free-space

*huyanwen@jnu.edu.cn
†fushenhe@jnu.edu.cn

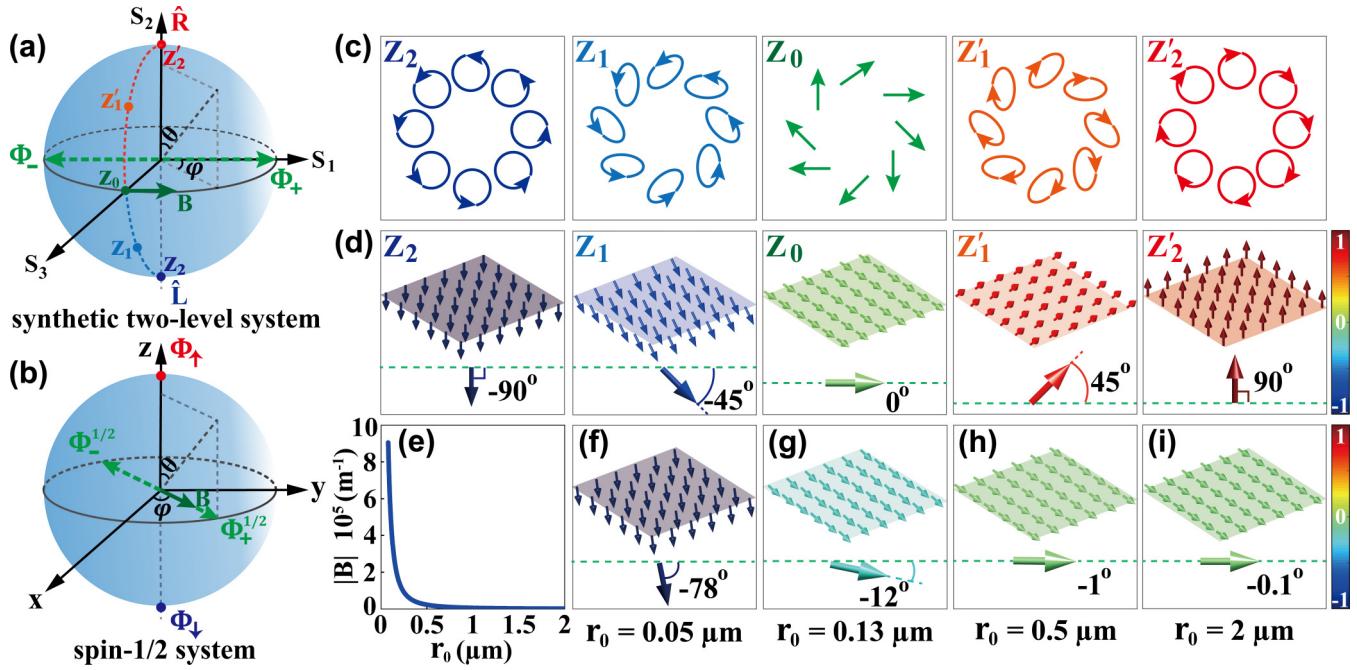

FIG. 1. (a) Geometrical representation of spin precession in the presence of SOC. $\hat{R}$ and $\hat{L}$ define the spin-up and -down equivalents in the B_2 direction, respectively; whereas Φ_+ and Φ_- denote two spin eigenstates in the direction of synthetic field **B**. Spin precession is initiated by a mixing spin $\Phi = 1/\sqrt{2}(\Phi_+ + i\Phi_-)$ located at z_0. (b) Bloch-sphere representation of spin-$\frac{1}{2}$ system, in the presence of external field **B**. $\Phi_\uparrow$ and $\Phi_\downarrow$ are spin up and down in the z direction, while $\Phi_+^{1/2}$ and $\Phi_-^{1/2}$ denote eigenstates of the system, corresponding to direction of **B**. (c) Polarization states mapped on a longitude line of the first-order ($\ell = 1$) sphere in (a). (d) Corresponding spin vectors to (c). (e) SOC strength as a function of beam width r_0. (f)–(i) Theoretical results for the spin vectors under actions of LG beam with different widths.

wave number with λ being the wavelength. $\Delta\beta = \beta_y - \beta_x$ is a phase mismatch. We define $\gamma_{x,y} = 1 - n_{x,y}^2/n_z^2$ as coupling parameters, related to crystal's polarity. The derivatives ∇_{xy}^2 and ∇_{yx}^2 in Eq. (1) stem from the nonzero term $\nabla \cdot \mathbf{E} \neq 0$, featuring origin of the SOC [41].

To address the rapid oscillation terms $\exp(\pm i\Delta\beta z)$, we transform the wave equation to a rotating form, by defining

$$E_x = \tilde{A}_x \exp(+i\Delta\beta z/2),$$
$$E_y = \tilde{A}_y \exp(-i\Delta\beta z/2), \tag{2}$$

respectively. Thus, a Hamiltonian of the system is written as

$$\mathbf{H} = \frac{1}{2\bar{\beta}}\begin{bmatrix} -\nabla_\perp^2 + \bar{\gamma}\nabla_{xx}^2, 0 \\ 0, -\nabla_\perp^2 + \bar{\gamma}\nabla_{yy}^2 \end{bmatrix} + \begin{bmatrix} \Delta\beta/2, \bar{\gamma}\nabla_{yx}^2/(2\bar{\beta}) \\ \bar{\gamma}\nabla_{xy}^2/(2\bar{\beta}), -\Delta\beta/2 \end{bmatrix}, \tag{3}$$

where $\nabla_\perp^2 = \nabla_{xx}^2 + \nabla_{yy}^2$ denotes the Laplace operator. We have assumed shallow crystal birefringence, namely, $\bar{\beta} \approx (\beta_x + \beta_y)/2$ and $\bar{\gamma} \approx (\gamma_x + \gamma_y)/2$. The second term in Eq. (3), which includes the derivative operators, couples the two polarization components. It means that the SOC is related to spatial structure of light.

We study the beam-dependent SOC in a synthetic two-level spin-orbit system. We define right and left circularly polarized vortex states as spin-up and -down equivalents in the z direction. They are written as [53–55]

$$\hat{R} = \exp(+i\ell\phi)(\hat{x} - i\hat{y})/\sqrt{2},$$
$$\hat{L} = \exp(-i\ell\phi)(\hat{x} + i\hat{y})/\sqrt{2}, \tag{4}$$

respectively, where $\hat{x}$ and $\hat{y}$ are unit vectors and $\phi = \arctan(y/x)$. Since the pseudospins are defined in the circular basis, the Hamiltonian is modified by a transformation from the Cartesian coordinate to the circular basis, yielding

$$\mathbf{H}' = \frac{\bar{\gamma} - 2}{4\bar{\beta}}\begin{bmatrix} \nabla_\perp^2, 0 \\ 0, \nabla_\perp^2 \end{bmatrix} + \begin{bmatrix} 0, \Delta\beta/2 - i\bar{\gamma}\nabla_{yx}^2/(2\bar{\beta}) \\ \Delta\beta/2 + i\bar{\gamma}\nabla_{yx}^2/(2\bar{\beta}), 0 \end{bmatrix}. \tag{5}$$

Given an overall field $\tilde{\mathbf{A}} = \tilde{A}(x, y, z)(\Phi_R\hat{R} + \Phi_L\hat{L})$, where Φ_R and Φ_L are weights on $\hat{R}$ and $\hat{L}$, respectively, we reduce Eq. (1) to the Schrödinger-type (Pauli) form

$$i\frac{\partial\Phi(z)}{\partial z} = \left(\frac{1}{2M}\mathbf{P}_\perp^2\tilde{A} - \frac{1}{2}\sigma\cdot\mathbf{B}\right)\Phi(z), \tag{6}$$

where $\Phi = (\Phi_R, \Phi_L)^{\mathrm{T}}$, $\mathbf{P}_\perp^2 = [-\nabla_\perp^2, 0; 0, -\nabla_\perp^2]$, and $M = 2\bar{\beta}\tilde{A}/(2 - \bar{\gamma})$. Here σ is the Pauli matrix vector. The SOC is described by a term $-\sigma\cdot\mathbf{B}$, where $B_1 = -\bar{\gamma}\nabla_{xy}^2\tilde{A}/(\bar{\beta}\tilde{A})$, $B_2 = 0$, and $B_3 = -\Delta\beta$. It is analogous to a coupling form which describes interaction between a particle's spin and its angular momentum in a moving frame [1,2]. More details refer to Appendix A. Since B_2 is zero, the vector **B** lies on the purely transverse B_1B_3 plane. The SOC Hamiltonian admits eigenstates that point to the vector **B** and comprise an equal superposition of $\hat{R}$ and $\hat{L}$, written as

$$\Phi_+ = 1/\sqrt{2}[\hat{R} + \exp(i\varphi)\hat{L}],$$
$$\Phi_- = 1/\sqrt{2}[\hat{R} - \exp(i\varphi)\hat{L}]. \tag{7}$$

Figure 1(a) visualizes the eigenstates and the pure states ($\hat{R}$ and $\hat{L}$) in the Poincaré sphere, showing close analogies

to Bloch-sphere representation of the spin-$\frac{1}{2}$ system [56,57] [Fig. 1(b)]. The spin states exhibit cylindrically symmetric polarization distributions. As illustration, Fig. 1(c) displays typical polarizations of states mapped onto a longitude line in the first-order ($\ell = 1$) sphere, while Fig. 1(d) depicts their corresponding spin vectors, represented by an angle $\arccos(S_2)$, where S_2 is value of polarization ellipticity. Since the state exhibits identical polarization ellipticity in the transverse plane, the resultant spin vectors are homogeneous.

The SOC term shows a dynamical effect, caused by the propagation-variant envelope $\tilde{A}$. This shows sharp contrast to conventional ones which are usually being independent terms. However, if optical diffraction is neglected, the dynamical behavior disappears and the SOC strongly relies on the envelope. In this scenario, a relevant beam parameter becomes an important degree of freedom for engineering the SOC. This is demonstrated in Fig. 1(e), showing close relationship between SOC strength and beam width in the phase-matching condition ($\Delta\beta = 0$). Here the Laguerre-Gaussian (LG) envelope is considered as

$$\tilde{A}(r) = \frac{r}{r_0}\exp\left(-\frac{r^2}{r_0^2}\right), \tag{8}$$

where $r = (x^2 + y^2)^{1/2}$, and r_0 features the beam width. At the deep-subwavelenth region ($r_0 < \lambda/2$), the SOC strength is rapidly increasing with a slight decrease of r_0. It becomes relatively negligible when $r_0 > \lambda$. This relation suggests that shrinking light to deep-subwavelength scale significantly enhances the SOC. Although the derivations are based on the slowly varying envelope approximation, the model can be applied to deep-subwavelength regime at the early stage of spin evolution.

To demonstrate the deep-subwavelength-induced SOC, we set the coupling length to be only one cycle ($z = \lambda$), such that a moderate SOC cannot cause obvious spin transport phenomenon. On the other hand, the SOC strength can be maintained during beam propagation, due to the short coupling length. This results in an adiabatic spin evolution, represented as a spin precession around $\mathbf{B}$, i.e.,

$$\frac{d\mathbf{S}}{dz} = \mathbf{B} \times \mathbf{S}, \tag{9}$$

where $\mathbf{S} = (S_1, S_2, S_3)$ is the state vector defined as $S_h = \Phi^\dagger \sigma_h \Phi$ ($h = 1, 2, 3$). The spin vector is therefore described by S_2. We initiate the spin precession from a mixing state: $\Phi = 1/\sqrt{2}[\Phi_+ + i\Phi_-]$. Figures 1(f)–1(i) display theoretical distributions of the spin vectors for different beam parameters. Evidently, for $r_0 = 0.05\,\mu$m, the spin rotates to an angle about -78°; by comparison, increasing the parameter to $r_0 = 0.13\ \mu$m causes less significant spin precession, manifested by a spin rotation angle about -12°. This indicates that the SOC strongly depends on the carrier envelope. Figures 1(h) and 1(i) show that a moderate SOC induced by the relatively larger envelope cannot cause spin precession.

III. EXPERIMENTAL RESULTS AND DISCUSSION

Experiments are carried out to confirm the predictions. A crucial ingredient is to generate the required spin-orbit state at the deep-subwavelength scale. This is challenging since the incident state cannot maintain its property after tightly focused by the high-numerical-aperture (NA) objective lens [58–60]. To overcome this problem, we fabricate a topology-preserving high-NA flat lens (the thickness is 60 nm) according to a technique reported in [61]. The flat lens [the layout is shown in Fig. 2(b)] has a NA up to 0.87 and a focal length of $z_f = 8\ \mu$m. A system comprising an objective lens (150×, NA=0.9) and a tube lens is utilized to characterize the flat lens [see Fig. 2(a)]. Figure 2(c) presents recorded intensity distribution of light at the focal plane. The focused LG beam exhibits a parameter of $r_0 \simeq 0.32\ \mu$m. The recorded regular interference [Fig. 2(d)] and y-polarization component [Fig. 2(e)] suggest that the expected initial spin is generated. Theoretical derivation about topology-preserving property of the flat lens (Appendix B) further confirms the generation.

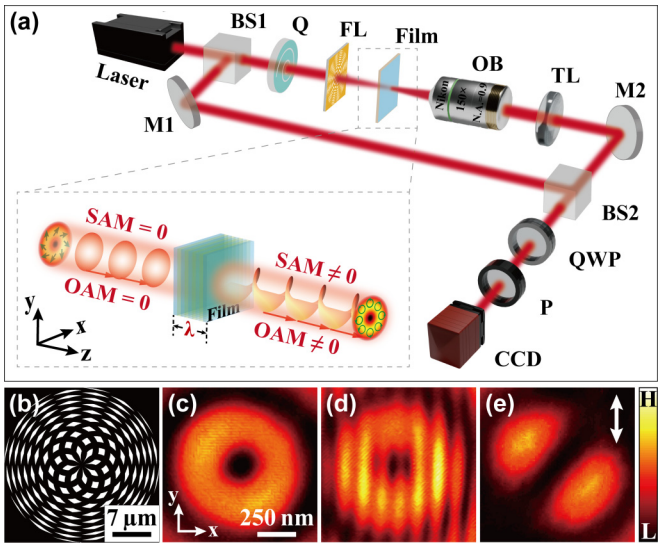

FIG. 2. (a) Experimental setup. BS: Beam splitter; Q: q plate; FL: Flat lens; M: Mirror; OB: Objective lens; TL: Tube lens; QWP: Quarter-wave plate; P: Polarizer; CCD: Charge-coupled device. The laser is operating at wavelength of $\lambda = 632.8$ nm. The insert in (a) shows that an equatorial mixing spin with equal weight on Φ_R and Φ_L is adiabatically converted to a pure spin down in the presence of the SOC. (b) Layout of the 60-nm-thick flat lens with NA=0.87. (c) Intensity distribution of the LG beam at the focal plane (z_f) of the flat lens. (d) Plane-wave interference and (e) y-polarization component of beam at z_f, indicating a generation of the expected spin state $\Phi = 1/\sqrt{2}(\Phi_+ + i\Phi_-)$. The scale bar in (c)–(e) is 250 nm. In color bar, L: Low; H: High.

An experimental setup is built for measuring the spin procession. A linearly polarized He-Ne laser ($\lambda = 632.8$ nm) is divided by a beam splitter. A q plate with a charge of $q = \frac{1}{2}$ is applied to transform the beam into expected spin state carrier by the LG envelope. The purity of the spin state from the q plate is measured as 95.2% (Appendix C). The LG beam is focused into deep-subwavelength region by the flat lens. A c-cut lithium niobate crystal film ($\bar{\gamma} = -0.08$) with a thickness about one wavelength is placed at the focal plane. The emerging beam, in the presence of the SOC, is expected to accumulate a nontrivial spin phenomenon [see the insert in Fig. 2(a)].

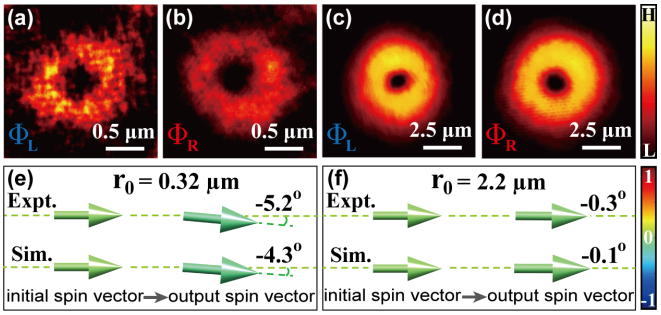

FIG. 3. Experimental observation of spin rotation induced by the deep-subwavelength LG beam ($r_0 = 0.32$ μm), as manifested by spin angular momentum conversion (flipping) from right-handed one (b) to the left-handed one (a). In comparison, a larger LG beam parameter $r_0 = 2.2$ μm is considered, resulting in balanced left-handed (c) and right-handed (d) components. (e), (f) The measured spin vectors before and after the crystal film, for (e) $r_0 = 0.32$ μm, and (f) $r_0 = 2.2$ μm. In the color bar (d), L: Low; H: High.

Figure 3 presents measurements confirming the spin precession. Since the spin is relevant to the circular polarization, we measure the right- (spin-↑) and left-handed (spin-↓) circular polarization components. These are achieved by rotating a quarter-wave plate to an angle of $-\pi/4$ and $+\pi/4$ with respect to x axis, respectively, while inserting a linear polarizer in front of the camera. Figures 3(a) and 3(b) depict intensity distributions of Φ_L and Φ_R, respectively. The measured Φ_L component is stronger than the Φ_R one, indicating a spin precession toward south pole of the sphere. Figure 3(e) shows the measured spin rotation by an angle of -5.2°, compared to the initial one [62]. This approximately matches to the simulated result. However, for a larger parameter ($r_0 = 2.2$ μm), the Φ_L and Φ_R components are approximately identical [Figs. 3(c) and 3(d)], meaning that the induced SOC is insufficient to flip the spin [Fig. 3(f)]. Slight difference between the experiment and theory can be mainly attributed to the imperfect LG envelope that is closely relevant to the derivative operator ∇^2_{xy} [62].

We observe nontrivial spin-precession phenomenon, manifested by a generation of the photonic OAM. Initially, both the SAM and OAM of state at the equator are zero. Under the action of the SOC, its intrinsic OAM and SAM are separated simultaneously. This nontrivial phenomenon is observed in Fig. 4(a), showing a clear dislocation in the plane-wave

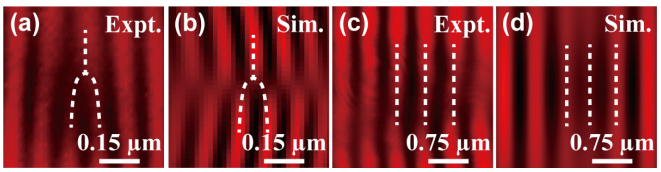

FIG. 4. Observation of the orbital-angular-momentum state induced by spin precession. (a), (c) The experimentally measured plane-wave interference patterns, for two different LG beam parameters: (a) $r_0 = 0.32$ μm, and (c) $r_0 = 2.2$ μm. (b), (d) The simulated [based on Eq. (1)] interference patterns corresponding to the measurements in (a) and (c). Experimental conditions are kept the same as those in Fig. 3.

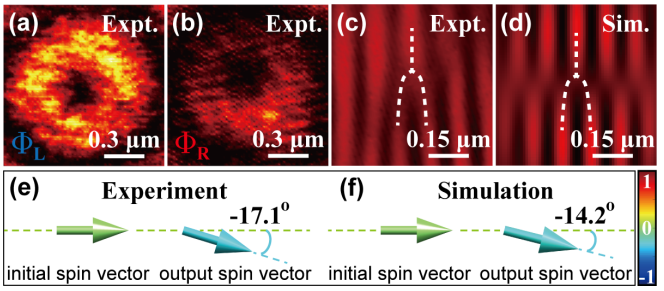

FIG. 5. Observation of the spin rotation by using the deep-subwavelength BG beam ($r_0 = 0.12$ μm). (a), (b) Experimentally measured intensity distributions of the left- and right-handed circular polarizations. (c), (d) Plane-wave interference patterns obtained both in experiment (c) and in simulation (d). (e), (f) The measured output spin rotation in comparison with the initial one: (e) experiment; (f) simulation.

interference fringes for the deep-subwavelength LG beam. This is a manifestation of wavefront helicity with a topological charge being $\ell = 1$. The spin precession accompanied by the OAM generation confirms the phenomenon of spin-orbit separation. This effect becomes negligible for larger envelope since the spin remains at its original position, as indicated by the regular interference fringes [Fig. 4(c)]. Theoretical results correspondingly shown in Figs. 4(b) and 4(d) are in accordance with the measurements.

We observe more prominent spin precession by considering the Bessel structured light with deeper-subwavelength feature size. The carrier envelope is replaced by

$$\tilde{A}(r) = J_\ell(r/r_0), \tag{10}$$

where J_ℓ denotes the Bessel function of order ℓ. In practice, we should properly truncate the ideal Bessel beam by using a Gaussian factor. The resultant Bessel-Gaussian (BG) profile exhibits nondiffracting property over a certain distance. We generate this BG beam using a metasurface whose geometry exhibits cylindrical symmetry. The highly localized BG beam is a result of in-phase interference of many high-spatial-frequency waves [51]. We demonstrate result for a beam parameter of $r_0 = 0.12$ μm, while maintaining other parameters unchanged. Similarly, an initial balance between the left- and right-handed components is broken by the SOC [Figs. 5(a) and 5(b)]. The output spin rotates to a larger angle of -17.1°, nearly in accordance with the theoretical calculation [Fig. 5(f)]. The measured and simulated interference patterns verify the spin-precession-induced OAM generation [see Figs. 5(c) and 5(d), respectively].

Finally, we propose to using the beam-dependent SOC in precision measurement of slight variation of structured light, with measurement accuracy up to 15 nm. This nanometric resolution is usually impossible to be reached by current optical detectors. It requires to realize rapid oscillation between the spin up and spin down. Specifically, we exploit the deep-subwavelength BG beam as carrier envelope of the spin. In this scenario, the Pauli equation [Eq. (6)] emulates a SOC process for the spin oscillation. Figure 6(a) depicts the

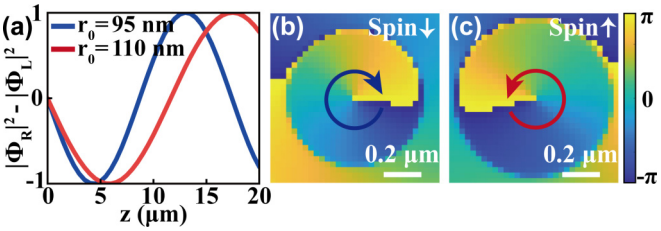

FIG. 6. (a) The simulated [based on Eq. (6)] beam-dependent spin oscillatory modes. (b), (c) The simulated [based on Eq. (1)] phase distributions of the output light states from the barium metaborate crystal film ($\bar{\gamma} = -0.16$), for (b) $r_0 = 95$ nm and (c) $r_0 = 110$ nm.

SOC-supported spin harmonic oscillations along with the coupling distance, for different cases of beam widths. Obviously, the spin oscillation is very sensitive to the change of spatial structure of light, giving rising to ultrasensitive beam-dependent oscillatory modes. As a result, a slight change of the beam width leads to significant spin flipping. This allows to detect the spatial variation of light as small as 15 nm. To verify the result, we present simulated outcomes [see Figs. 6(b) and 6(c)], clearly showing opposite helical wavefronts of the output states (corresponding to the spin down and spin up), for $r_0 = 95$ nm and $r_0 = 110$ nm. Note that one can further increase the measuring sensitivity by properly reducing the beam width.

IV. CONCLUSION

In summary, we have demonstrated both theoretically and experimentally SOC phenomena caused by the deep-subwavelength spin-orbit structured light. This beam-dependent SOC contrasts to those being material dependent [44,45]. The reported SOC is closely relevant to the spatial gradient of light field, hence, it can be significantly enhanced by using the deep-subwavelength carrier envelopes. We have qualitatively characterized this effect, by measuring the spin precessions under different beam parameters. Particularly, based on the deep-subwavelength Bessel beam, a significant spin rotation about -17.1°, accompanied by OAM generation, was achieved within a coupling length of only one wavelength. The influence of the phase mismatch on the beam-dependent SOC was also discussed (see Appendix D). These fundamental SOC phenomena may find interesting applications in different areas [63–66]. As an example, we have proposed to use such a strong SOC effect in the precise measurement of slight spatial change of light with nanometric resolution.

ACKNOWLEDGMENTS

We thank B. Malomed from Tel Aviv University for kind discussions about the SOC. This work was supported by the National Natural Science Fundation of China (Grants No. 62175091 and No. 12304358), and the Guangzhou science and technology project (Project No. 202201020061).

APPENDIX A: ANALOGY OF SPIN-ORBIT COUPLING IN SPIN-$\frac{1}{2}$ SYSTEM AND SYNTHETIC TWO-LEVEL SYSTEM

The spin-$\frac{1}{2}$ dynamics in the external vector field $\mathbf{B}$ can be described by a Hamiltonian term $\mathbf{H_{1/2}} = \sigma \cdot \mathbf{B}$, where σ is the Pauli matrix vector. In a normalized form, it can be expressed as

$$\mathbf{H_{1/2}} = \frac{1}{2}\begin{bmatrix} \cos\theta & \sin\theta\exp(-i\varphi) \\ \sin\theta\ \exp(i\varphi) & -\cos\theta \end{bmatrix}, \tag{A1}$$

where θ and φ are two angles that define a normalized (unit) sphere. The vector $\mathbf{B}$ then possesses around the sphere, with direction determined by θ and φ. This Hamiltonian $\mathbf{H_{1/2}}$ admits two spin eigenstates that point along to $\mathbf{B}$, written as

$$\begin{aligned} \Phi_+^{1/2} &= \cos\left(\frac{\theta}{2}\right)\Phi_\uparrow + \exp(i\varphi)\sin\left(\frac{\theta}{2}\right)\Phi_\downarrow, \\ \Phi_-^{1/2} &= \sin\left(\frac{\theta}{2}\right)\Phi_\uparrow - \exp(i\varphi)\cos\left(\frac{\theta}{2}\right)\Phi_\downarrow, \end{aligned} \tag{A2}$$

where $\Phi_\uparrow = [1 \quad 0]^{\mathrm{T}}$ and $\Phi_\downarrow = [0 \quad -1]^{\mathrm{T}}$ are spin-up and -down states defined in the z direction. Figure 1(b) geometrically depicts this picture onto a Bloch sphere. All possible spins of the system can now be mapped onto the sphere, with the spin up $\Phi_\uparrow$ and spin down $\Phi_\downarrow$ located at the north and south poles of the sphere, respectively. In the presence of the external field $\mathbf{B}$, the initial spin precesses around the vector $\mathbf{B}$, giving rise to many intriguing spin transport phenomena such as the geometric phase.

In our case, we study spin-orbit coupling of structured light in a photonic crystal. The structured light in the system is comprising a superposition of two orthogonal spin-orbit states with nontrivial topological structures. They can be written as $\hat{R} = \exp(il\phi)(\hat{x} - i\hat{y})/\sqrt{2}$ and $\hat{L} = \exp(-il\phi)(\hat{x} + i\hat{y})/\sqrt{2}$, respectively. These topological states define the spin-up and -down equivalents along the z axis, respectively, but they are not eigenstates of the analogous spin-orbit Hamiltonian $\mathbf{H_{soc}} = -\sigma \cdot \mathbf{B}$. In the circular basis, a similar Hamiltonian matrix can be written as

$$\mathbf{H_{soc}} = \begin{bmatrix} B_2 & B_3 - iB_1 \\ B_3 + iB_1 & -B_2 \end{bmatrix}. \tag{A3}$$

In our case, since B_2 is zero (see the main text), the effective vector $\mathbf{B}$ obtained here lies on the purely transverse B_1B_3 plane, as shown in Fig. 1(a). As a result, the pseudospin eigenstates of $\mathbf{H_{soc}}$ that point along this transverse vector $\mathbf{B}$ comprise an equal superposition of $\hat{R}$ and $\hat{L}$, express as

$$\begin{aligned} \Phi_+ &= \cos\left(\frac{\pi}{4}\right)\hat{R} + \exp(i\varphi)\sin\left(\frac{\pi}{4}\right)\hat{L}, \\ \Phi_- &= \sin\left(\frac{\pi}{4}\right)\hat{R} - \exp(i\varphi)\cos\left(\frac{\pi}{4}\right)\hat{L}. \end{aligned} \tag{A4}$$

We can now interpret these eigenstates as a mixing of $\hat{R}$ and $\hat{L}$. Poincaré-sphere representation allows us to visualize these spin eigenstates as well as the pure states $\hat{R}$ and $\hat{L}$. Clearly, this is analogous to the Bloch-sphere representation for the spin-$\frac{1}{2}$ system. The spin-orbit coupling makes this state evolve along the Poincaré sphere, which can be described by the synthetic

TABLE I. Analogies between the presented synthetic spin-$\frac{1}{2}$ system in the higher-order optical regime and the spin-$\frac{1}{2}$ system in the quantum mechanics. The direct analogies between these two different settings enable us to emulate intriguing spin transport phenomena in the presence of spin-orbit coupling.

Physical parameters	Spin-$\frac{1}{2}$ system	Synthetic spin-$\frac{1}{2}$ system
Spins	$\Phi_{\uparrow}$ and $\Phi_{\downarrow}$	$\hat{R}$ and $\hat{L}$
Eigenstates	$\Phi_{+}^{1/2}$ and $\Phi_{-}^{1/2}$	Φ_{+} and Φ_{-}
Field vector	$\mathbf{B}$ (real)	$\mathbf{B}$=$[-\bar{\gamma}/(\tilde{\beta}\tilde{A})\nabla_{xy}^2\tilde{A}, 0, -\Delta\beta]$
Spin-orbit coupling term	$\mathbf{H_{1/2}} = \sigma \cdot \mathbf{B}$	$\mathbf{H_{SOC}} = \sigma \cdot \mathbf{B}$
Space/time coordinates	(x, y, t)	(x, y, z)
Mass	m	$M = 2\tilde{\beta}\tilde{A}/(2-\bar{\gamma})$
Momentum operator	$\mathbf{P}_{\perp}^2 = [-\nabla_{\perp}^2, 0; 0, -\nabla_{\perp}^2]$	$\mathbf{P}_{\perp}^2 = [-\nabla_{\perp}^2, 0; 0, -\nabla_{\perp}^2]$

Pauli equation

$$i\frac{\partial\Phi}{\partial z} = \left(\frac{1}{2M}\mathbf{P}_{\perp}^2\tilde{A} - \frac{1}{2}\sigma\cdot\mathbf{B}\right)\Phi. \tag{A5}$$

Table I summarizes analogous formulas between these two systems.

APPENDIX B: THEORETICAL DERIVATION FOR THE TOPOLOGY-PRESERVING FLAT LENS

In this Appendix, we theoretically prove that the flat lens used in the experiment does not change the spin-orbit property of the LG beam after tightly focusing. The flat lens is designed by an amplitude-only hologram generated from an interference between an angular cosine wave and a spherical wave (see Ref. [61] in the text). When the LG beam $\tilde{A}(x, y)$ carrying a general spin state Φ passes through the flat lens, it is modulated in binary. As a result, the light field behind the flat lens can be expressed as

$$\mathbf{E}(x, y, z = 0) = \tilde{A}(x, y)\cdot t(x, y)[\Phi_x(\phi)\hat{x} + \Phi_y(\phi)\hat{y}], \tag{B1}$$

where $t(x, y)$ denotes transmission function of the flat lens and $\phi = \arctan(y/x)$. Within this initial condition, we solve the diffractive problem according to the vectorial Helmholtz wave equation. The diffractive field at the focal plane of the flat lens can be written as

$$\mathbf{E}(x, y, z_f) = \frac{k}{i2\pi z_f}\iint \mathbf{E}(x', y', z = 0) \times \exp\left\{\frac{ik}{2z_f}[(x - x')^2 + (y - y')^2]\right\}dx'dy'. \tag{B2}$$

Note that owing to the cylindrical symmetry of the flat lens [see the layout in the text, Fig. 2(b)], the transmission function can be also given in a cylindrical form of $t(r)$, where $r = (x^2 + y^2)^{1/2}$. In this case, the complex amplitude of the initial field is separable in the polar coordinates (r, ϕ). We therefore rewrite the solution in the cylindrical coordinate system and deal with the integrals. We finally obtain the analytical solution for the vectorial light field at the focal plane, given by

$$\mathbf{E}(x, y, z_f) = f(r)[\Phi_x(\phi)\hat{x} + \Phi_y(\phi)\hat{y}], \tag{B3}$$

where

$$f(r) = -\frac{k}{z_f}\int_0^{\infty}\tilde{A}(r')t(r')r'J_1\left(\frac{krr'}{z_f}\right) \times \exp\left[\frac{ik}{2z_f}(r^2 + r'^2)\right]dr' \tag{B4}$$

and J_1 indicates the first-order Bessel function. It is evident that the diffractive field at the focal plane shares a similar analytic form to the initial one, except for that the envelope becomes a z-dependent function. It indicates that the flat lens can completely retain the initial spin state when it is focused into the input end of the crystal. The topology-preserving flat lens enables us to detect the pseudospin precession caused by the deep-subwavelength structured light, which cannot be achieved by using the conventional high-NA objective lens.

APPENDIX C: PURITY MEASUREMENT OF THE FIRST-ORDER LG BEAM FROM THE q PLATE

We perform additional experiment to show that the generated first-order LG beam from the q plate is of high purity, which is sufficiently enough to detect the photonic spin-orbit coupling effect. We utilize a modal decomposition method [67,68] to measure the purities of the output LG mode from the q plate with a topological charge of $q = \frac{1}{2}$ [see an

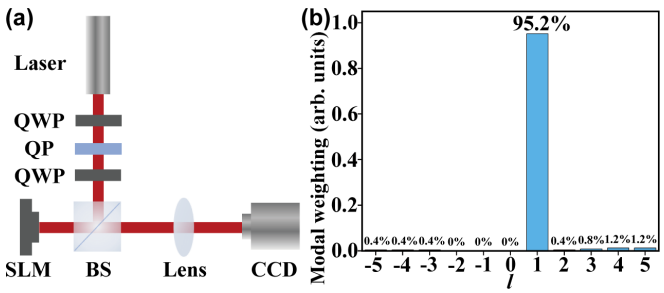

FIG. 7. Modal decomposition results. (a) An experimental setup used to measure the purity of the first-order LG beam emerging from the q plate. The LG beam is decomposed into LG basis modes. The linearly polarized He-Ne laser operating at the wavelength of 632.8 nm is considered. QWP, quarter-wave plate; QP, q plate with a topological number of $q = \frac{1}{2}$; SLM, spatial light modulator; BS, beam splitter; CCD, charge-coupled device. (b) The modal decomposition results at the basis of LG modes with topological charge ranging from $l = -5$ to 5.

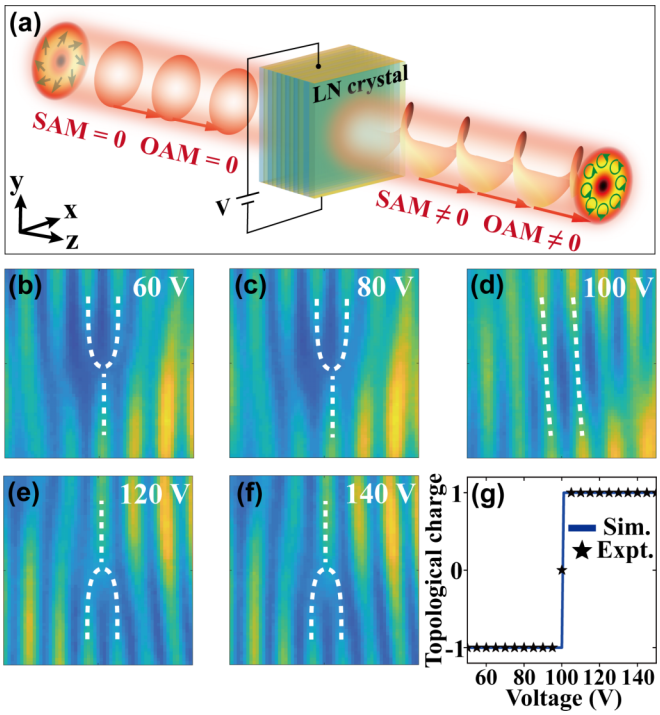

FIG. 8. Controllable spin-orbit coupling by engineering the phase mismatch in a c-cut electro-optic lithium niobate crystal. (a) Experimental scheme for observing the electrically engineered spin-orbit coupling. (b)–(f) Experimentally measured photonic spin states at different applied voltages: (b) U=60 V, (c) U=80 V, (d) U=100 V, (e) U=120 V, and (f) U=140 V. (g) The measured topological charge as a function of applied voltage. Sim: Simulation; Expt: Experiment. In this experiment, the coupling length of the crystal is set to $z = 30$ mm.

experimental setup in Fig. 7(a)]. Two quarter-wave plates (QWPs) are used to select a proper polarization of the generated first-order ($l = 1$) LG beam that matches to the spatial light modulator (SLM). A group of pure LG modes generated from digital holograms by using the SLM are considered to decompose the LG beam. Figure 7(b) shows the decomposing result depicted in a histogram. It is seen that the measured purity of the first-order LG beam from the q plate is 95.2%.

APPENDIX D: ENGINEERING PHOTONIC SPIN-ORBIT COUPLING BY TUNING THE PHASE MISMATCH

In addition to the beam-dependent photonic spin-orbit coupling which we have shown in the main text, we perform additional experiments confirming that the spin-orbit coupling can be also controlled by engineering the phase mismatch. To this end, we consider electrically tuning the phase mismatch in a c-cut electro-optic lithium niobate (LN) crystal, whose optical axis is in accordance with propagation direction of the beam [see Fig. 8(a)]. In the presence of transverse modulation, the phase mismatch can be written as

$$\Delta\beta = -k_0 n_o^3 \gamma_{22} U/d, \tag{D1}$$

where $k_0 = 2\pi/\lambda$ denotes wave number in vacuum with λ being wavelength, n_o is the ambient refractive index of the crystal, U is the applied voltage, d is the thickness, and $\gamma_{22} = 6.8$ pm/V is an electro-optic coefficient of the crystal. In this case, the external knob U is utilized to finely tune the phase mismatch and the resulting spin-orbit coupling. We use the same experimental setup and obtain a voltage-dependent transition between different spin states in the phase-mismatching regime. Figures 8(b)–8(f) show controllable spin states of light by varying the applied voltage. Moreover, we perform detailed experiments to measure the topological charge of the output light state as a function of voltage [see Fig. 8(g)]. These results suggest another important degree of freedom for engineering the spin-orbit coupling.

[1] R. Winkler, *Spin-Orbit Coupling Effects in Two-Dimensional Electron and Hole Systems*, Springer Tracts in Modern Physics Vol. 191 (Springer, New York, 2003).

[2] M. Aidelsburger, S. Nascimbene, and N. Goldman, Artifical gauge fields in materials and engineered systems, C. R. Phys. **19**, 394 (2018).

[3] Y.-J. Lin, K. Jiménez-García, and I. B. Spielman, Spin-orbit-coupled Bose-Einstein condensates, Nature (London) **471**, 83 (2011).

[4] V. Galitski and I. B. Spielman, Spin-orbit coupling in quantum gases, Nature (London) **494**, 49 (2013).

[5] Y. K. Kato, R. C. Myers, A. C. Gossard, and D. D. Awschalom, Observation of the spin Hall effect in semiconductors, Science **306**, 1910 (2004).

[6] M. Z. Hasan and C. L. Kane, *Colloquium*: Topological insulators, Rev. Mod. Phys. **82**, 3045 (2010).

[7] M. Hafezi, E. A. Demler, M. D. Lukin, and J. M. Taylor, Robust optical delay lines with topologial protection, Nat. Phys. **7**, 907 (2011).

[8] K. Y. Bliokh, F. J. Rodríguez-Fortuño, F. Nori, and A. V. Zayats, Spin-orbit interactions of light, Nat. Photonics **9**, 796 (2015).

[9] A. T. O'Neil, I. MacVicar, L. Allen, and M. J. Padgett, Intrinsic and extrinsic nature of the orbital angular momentum of a light beam, Phys. Rev. Lett. **88**, 053601 (2002).

[10] L. Allen, M. W. Beijersbergen, R. J. C. Spreeuw, and J. P. Woerdman, Orbital angular momentum of light and the transformation of Laguerre-Gaussian laser modes, Phys. Rev. A **45**, 8185 (1992).

[11] M. Onoda, S. Murakami, and N. Nagaosa, Hall effect of light, Phys. Rev. Lett. **93**, 083901 (2004).

[12] A. Kavokin, G. Malpuech, and M. Glazov, Optical spin Hall effect, Phys. Rev. Lett. **95**, 136601 (2005).

[13] O. Hosten and P. Kwiat, Observation of the spin Hall effect of light via weak measurements, Science **319**, 787 (2008).

[14] S. Fu, C. Guo, G. Liu, Y. Li, H. Yin, Z. Li, and Z. Chen, Spin-orbit optical Hall effect, Phys. Rev. Lett. **123**, 243904 (2019).

[15] L. Marrucci, C. Manzo, and D. Paparo, Optical spin-to-orbital angular momentum conversion in inhomogeneous anisotropic media, Phys. Rev. Lett. **96**, 163905 (2006).

[16] Y. Zhao, J. S. Edgar, G. D. M. Jeffries, D. McGloin, and D. T. Chiu, Spin-to-orbital angular momentum conversion in a strongly focused optical beam, Phys. Rev. Lett. **99**, 073901 (2007).
[17] Y. Gorodetski, A. Niv, V. Kleiner, and E. Hasman, Observation of the spin-based plasmonic effect in nanoscale structures, Phys. Rev. Lett. **101**, 043903 (2008).
[18] N. Shitrit, I. Yulevich, E. Maguid, D. Ozeri, D. Veksler, V. Kleiner, and E. Hasman, Spin-optical metamaterial route to spin-controlled photonics, Science **340**, 724 (2013).
[19] L. Fang, H. Wang, Y. Liang, H. Cao, and J. Wang, Spin-orbit mapping of light, Phys. Rev. Lett. **127**, 233901 (2021).
[20] N. Levy, S. A. Burke, K. L. Meaker, M. Panlasigul, A. Zettl, F. Guinea, A. H. C. Neto, and M. F. Crommie, Strain-induced pseudo-magnetic fields greater than 300 Tesla in graphene nanobubbles, Science **329**, 544 (2010).
[21] T. Low and F. Guinea, Strain-induced pseudomagnetic field for novel graphene electronics, Nano Lett. **10**, 3551 (2010).
[22] F. de Juan, A. Cortijo, M. A. H. Vozmediano, and A. Cano, Aharonov-Bohm interferences from local deformations in graphene, Nat. Phys. **7**, 810 (2011).
[23] F. Guinea, M. I. Katsnelson, and A. K. Geim, Energy gaps and a zero-field quantum Hall effect in graphene by strain engineering, Nat. Phys. **6**, 30 (2010).
[24] K. I. Bolotin, F. Ghahari, M. D. Shulman, H. L. Stormer, and P. Kim, Observation of the fractional quantum Hall effect in graphene, Nature (London) **462**, 196 (2009).
[25] M. C. Rechtsman, J. M. Zeuner, A. Tünnermann, S. Nolte, M. Segev, and A. Szameit, Strain-induced pseudomagnetic field and photonic Landau levels in dielectric structures, Nat. Photonics **7**, 153 (2013).
[26] Y. Lumer, M. A. Bandres, M. Heinrich, L. J. Maczewsky, H. Herzig-Sheinfux, A. Szameit, and M. Segev, Light guiding by artificial gauge fields, Nat. Photonics **13**, 339 (2019).
[27] R. O. Umucalılar and I. Carusotto, Artificial gauge field for photons in coupled cavity arrays, Phys. Rev. A **84**, 043804 (2011).
[28] S. Longhi, Effective magnetic field for photons in waveguide and coupled resonator lattices, Opt. Lett. **38**, 3570 (2013).
[29] K. Fang, Z. Yu, and S. Fan, Realizing effective magnetic field for photons by controlling the phase of dynamic modulation, Nat. Photonics **6**, 782 (2012).
[30] K. Fang, Z. Yu, and S. Fan, Photonic Aharonov-Bohm effect based on dynamic modulation, Phys. Rev. Lett. **108**, 153901 (2012).
[31] K. Fang and S. Fan, Controlling the flow of light using the inhomogeneous effective gauge field that emerges from dynamic modulation, Phys. Rev. Lett. **111**, 203901 (2013).
[32] M. Król, K. Rechcińska, H. Sigurdsson, P. Oliwa, R. Mazur, P. Morawiak, W. Piecek, P. Kula, P. G. Lagoudakis, M. Matuszewski, W. Bardyszewski, B. Pietka, and J. Szczytko, Realizing optical persistent spin helix and Stern-Gerlach defection in an anisotropic liquid crystal microcavity, Phys. Rev. Lett. **127**, 190401 (2021).
[33] F. Liu and J. Li, Gauge field optics with anisotropic media, Phys. Rev. Lett. **114**, 103902 (2015).
[34] V. G. Sala, D. D. Solnyshkov, I. Carusotto, T. Jacqmin, A. Lemaître, H. Terças, A. Nalitov, M. Abbarchi, E. Galopin, I. Sagnes, J. Bloch, G. Malpuech, and A. Amo, Spin-orbit coupling for photons and polaritons in microstructures, Phys. Rev. X **5**, 011034 (2015).
[35] S. Ma, H. Jia, Y. Bi, S. Ning, F. Guan, H. Liu, C. Wang, and S. Zhang, Gauge field induced chiral zero mode in five-dimensional Yang monopole metamaterials, Phys. Rev. Lett. **130**, 243801 (2023).
[36] Q. Yan, Z. Wang, D. Wang, R. Ma, C. Lu, G. Ma, X. Hu, and Q. Gong, Non-Abelian gauge field in optics, Adv. Opt. Photon. **15**, 907 (2023).
[37] O. Yesharim, A. Karnieli, S. Jackel, G. Di Domenico, S. Trajtenberg-Mills, and A. Arie, Observation of the all-optical Stern-Gerlach effect in nonlinear optics, Nat. Photonics **16**, 582 (2022).
[38] A. Karnieli and A. Arie, All-optical Stern-Gerlach effect, Phys. Rev. Lett. **120**, 053901 (2018).
[39] G. Liu, S. Fu, S. Zhu, H. Yin, Z. Li, and Z. Chen, Higher-order optical Rabi oscillations, Fund. Res. **3**, 898 (2023).
[40] A. Tomita and R. Y. Chiao, Observation of Berry's topological phase by use of an optical fiber, Phys. Rev. Lett. **57**, 937 (1986).
[41] V. S. Liberman and B. Y. Zel'dovich, Spin-orbit interaction of a photon in an inhomogeneous medium, Phys. Rev. A **46**, 5199 (1992).
[42] Y. V. Kartashov, B. A. Malomed, V. V. Konotop, V. E. Lobanov, and L. Torner, Stabilization of spatiotemporal solitons in Kerr media by dispersive coupling, Opt. Lett. **40**, 1045 (2015).
[43] H. Sakaguchi and B. A. Malomed, One- and two-dimensional solitons in PT-symmetric systems emulating spin-orbit coupling, New J. Phys. **18**, 105005 (2016).
[44] C. Mann, S. A. R. Horsley, and E. Mariani, Tunable pseudomagnetic fields for polaritons in strained metasurfaces, Nat. Photonics **14**, 669 (2020).
[45] K. Rechcińska, M. Król, R. Mazur, P. Morawiak, R. Mirek, K. Łempicka, W. Bardyszewski, M. Matuszewski, P. Kula, W. Piecek, P. G. Lagoudakis, B. Piętka, and J. Szczytko, Engineering spin-orbit synthetic Hamiltonians in liquid-crystal optical cavities, Science **366**, 727 (2019).
[46] A. Forbes, M. de Oliveira, and M. R. Dennis, Structured light, Nat. Photonics **15**, 253 (2021).
[47] Y. Shen, X. Wang, Z. Xie, C. Min, X. Fu, Q. Liu, M. Gong, and X. Yuan, Optical vortices 30 years on: OAM manipulation from topological charge to multiple singularities, Light: Sci. Appl. **8**, 90 (2019).
[48] J. Jia, H. Lin, Y. Liao, Z. Li, Z. Chen, and S. Fu, Pendulum-type light beams, Optica **10**, 90 (2023).
[49] A. F. Koenderink, Andrea Alù, and A. Polman, Nanophotonics: Shrinking light-based technology, Science **348**, 516 (2015).
[50] Y. Hu, S. Wang, J. Jia, S. Fu, H. Yin, Z. Li, and Z. Chen, Optical superoscillatory waves without side lobes along a symmetric cut, Adv. Photonics **3**, 045002 (2021).
[51] Y. Hu, S. Fu, H. Yin, Z. Li, Z. Li, and Z. Chen, Subwavelength generation of nondiffracting structured light beams, Optica **7**, 1261 (2020).
[52] C. Guo, S. Fu, H. Lin, Z. Li, H. Yin, and Z. Chen, Dynamic control of cylindrical vector beams via anisotropy, Opt. Express **26**, 18721 (2018).
[53] Y. Hu, G. Mo, Z. Ma, S. Fu, S. Zhu, H. Yin, Z. Li, and Z. Chen, Vector vortex state preservation in Fresnel cylindrical diffraction, Opt. Lett. **46**, 1313 (2021).
[54] D. Naidoo, F. S. Roux, A. Dudley, I. Litvin, B. Piccirillo, L. Marrucci, and A. Forbes, Controlled generation of higher-order

Poincaré sphere beams from a laser, Nat. Photonics **10**, 327 (2016).

[55] G. Milione, H. I. Sztul, D. A. Nolan, and R. R. Alfano, Higher-order Poincaré sphere, stokes parameters, and the angular momentum of light, Phys. Rev. Lett. **107**, 053601 (2011).

[56] M. O. Scully, W. E. Lamb, Jr., and A. Barut, On the theory of the Stern-Gerlach apparatus, Found. Phys. **17**, 575 (1987).

[57] M. V. Berry, The adiabatic phase and Pancharatnam's phase for polarized light, J. Mod. Opt. **34**, 1401 (1987).

[58] R. Dorn, S. Quabis, and G. Leuchs, Sharper focus for a radially polarized light beam, Phys. Rev. Lett. **91**, 233901 (2003).

[59] X. Xie, Y. Chen, K. Yang, and J. Zhou, Harnessing the point-spread function for high-resolution far-field optical microscopy, Phys. Rev. Lett. **113**, 263901 (2014).

[60] H. Wang, L. Shi, B. Lukyanchuk, C. Sheppard, and C. T. Chong, Creation of a needle of longitudinally polarized light in vacuum using binary optics, Nat. Photonics **2**, 501 (2008).

[61] X. Zhang, Y. Hu, X. Zhang, S. Zhu, H. Yin, Z. Li, Z. Chen, and S. Fu, A global phase-modulation mechanism for flat-lens design, Adv. Opt. Mater. **10**, 2202270 (2022).

[62] In experiment, the spin rotation was obtained by measuring $S_2 = |\Phi_R|^2 - |\Phi_L|^2$. Ideally, the spatial distribution of S_2 is homogeneous; whereas in experiment it exhibits fluctuations due to the imperfect beam envelope. We therefore average it by using an expression $\bar{S}_2 = \sum_n^{N_x} \sum_m^{N_y} S_{2,n,m}/(N_x N_y)$.

[63] M. Mirhosseini, M. Malik, Z. Shi, and R. W. Boyd, Efficient separation of the orbital angular momentum eigenstates of light, Nat. Commun. **4**, 2781 (2013).

[64] J. Chen, C. Wan, and Q. Zhan, Engineering photonic angular momentum with structured light: A review, Adv. Photonics **3**, 064001 (2021).

[65] R. Vijay, C. Macklin, D. H. Slichter, S. J. Weber, K. W. Murch, R. Naik, A. N. Korotkov, and I. Siddiqi, Stabilizing Rabi oscillations in a superconducting qubit using quantum feedback, Nature (London) **490**, 77 (2012).

[66] G. Cronenberg, P. Brax, H. Filter, P. Geltenbort, T. Jenke, G. Pignol, M. Pitschmann, M. Thalhammer, and H. Abele, Acoustic Rabi oscillations between gravitational quantum states and impact on symmetron dark energy, Nat. Phys. **14**, 1022 (2018).

[67] C. Schulze, A. Dudley, D. Flamm, M. Duparré, and A. Forbes, Measurement of the orbital angular momentum density of light by modal decomposition, New J. Phys. **15**, 073025 (2013).

[68] D. Wei, Y. Cheng, R. Ni, Y. Zhang, X. Hu, S. Zhu, and M. Xiao, Generating controllable Laguerre-Gaussian laser modes through intracavity spin-orbital angular momentum conversion of light, Phys. Rev. Appl. **11**, 014038 (2019).